



Long-lived and multiplexed atom-photon entanglement interface with feed-forward-controlled readouts

Sheng-zhi Wang^{1,2}, Min-jie Wang^{1,2}, Ya-fei Wen^{1,2}, Zhong-xiao Xu^{1,2}, Teng-fei Ma^{1,2}, Shu-jing Li^{1,2} & Hai Wang^{1,2}  

Quantum interfaces (QIs) that generate entanglement between photonic and spin-wave (atomic memory) qubits are basic building block for quantum repeaters. Realizing ensemble-based repeaters in practice requires quantum memory providing long lifetimes and multi-mode capacity. Significant progress has been achieved on these separate goals. The remaining challenge is to combine the two attributes into a single QI. Here, by establishing spatial multimode, magnetic-field-insensitive and long-wavelength spin-wave storage in laser-cooled atoms inside a phase-passively-stabilized polarization interferometer, we constructed a multiplexed QI that stores up to three long-lived spin-wave qubits. Using a feed-forward-controlled system, we demonstrated that a multiplexed QI gives rise to a 3-fold increase in the atom-photon (photon-photon) entanglement-generation probability compared with single-mode QIs. For our multiplexed QI, the measured Bell parameter is 2.51 ± 0.01 combined with a memory lifetime of up to 1 ms. This work represents a key step forward in realizing fiber-based long-distance quantum communications.

¹The State Key Laboratory of Quantum Optics and Quantum Optics Devices, Institute of Opto-Electronics, Shanxi University, 030006 Taiyuan, China.

²Collaborative Innovation Center of Extreme Optics, Shanxi University, 030006 Taiyuan, China. ✉email: wanghai@sxu.edu.cn

Quantum repeaters (QRs)¹ hold promise for distributing entanglement over long distances (>1000 km) via optical fibers, thereby providing a feasible path to realize long-distance quantum communications^{2–4} and quantum networks^{5,6}. In QRs, long distances are divided into short elementary links, with each link comprising two nodes that store quantum states^{1–4}. For each link, entanglement between the two nodes is required to be established in a “heralded” way^{2,7}. Various physical systems⁸ such as atomic ensembles^{2,4,9} and single quantum systems, including single atoms^{10,11}, ions^{12,13} and solid-state spins^{14,15} have been proposed as nodes. The atomic-ensemble-based nodes, which were initially proposed in the Duan–Lukin–Cirac–Zoller (DLCZ) protocol⁴, are formed by quantum interface (QIs) that create quantum correlations between a spin wave (SW) and a photon via spontaneous Raman emissions (SREs) induced by a write pulse^{2,16–29}. The quantum correlations created via SREs form the basis of generating entanglement between a photonic qubit and a SW qubit^{2,30–33}. Ensemble-based QIs are attractive because a large number of atoms ensure an efficient quantum memory (QM)^{2,19,20}. In an improved DLCZ scheme^{34,35}, the QR uses SW–photon entanglement (SWPE) instead of quantum correlations as nodes, thereby removing the requirement for long-distance phase stability in the original DLCZ protocol³⁶. Over the past decade, QIs that generate SW–photon (atom–photon) entanglement through SREs^{30–33,37–42} or storage of photonic entanglement^{43–45} in atomic ensembles have been demonstrated. With atom–photon entanglement, quantum teleportation from photon^{46,47} or matter⁴⁸ to matter and elementary entanglement generations^{36,49} have been demonstrated.

In QRs, QMs are required to have long lifetimes to store the generated entanglement in elementary links^{2,3,7,50,51}. To achieve long-lived DLCZ-like QMs, the decoherence of SWs in cold atomic ensembles has been widely studied^{21–27,38}. Atomic motions and inhomogeneous broadening of the spin transitions were shown to cause SW dephasing. Motion-induced decoherence was suppressed either using an approximately collinear configuration^{23,24} or confining the atoms in optical lattices^{25–27,38}, where the approximately collinear configuration requires the angle of the Stokes propagation direction relative to the write beam to be small and a long-wavelength SW to be attained²³. Inhomogeneous-broadening-induced decoherence may be reduced using magnetic-field-insensitive coherences in SW storage^{23–27,38}. Long-lived (0.1 s) and non-multiplexed atom–photon entanglement was demonstrated in optical-lattice atoms³⁸, in which the memory qubit was stored as two spatially-distinct SWs, both associated with the $0 \leftrightarrow 0$ magnetic-field-insensitive coherence, and the corresponding photonic qubit encoded into two arms of a Mach–Zehnder interferometer. However, to maintain maximal entanglement, the relative phase between the arms was actively stabilized to zero by coupling an auxiliary laser beam into the interferometer³⁸.

DLCZ-type QRs using single-mode memory have very slow repeater rates for practical use^{2,52–56}. To overcome this problem, multiplexed versions of the DLCZ schemes were proposed^{2,7,54–58}. Multimode quantum storages of single SWs have been mainly implemented with rare-earth-ion-doped (REID) crystals^{59–62} or cold atoms^{58,63–71}. With REID crystals, spin-wave-photon quantum correlations in more than 10 temporal modes have been demonstrated^{59,60} via the DLCZ approach. The longest quantum-correlation storage time was pushed to 1 ms applying spin-echo operations⁵⁹. However, the values of the cross-correlation function at storage times 0.5 and 1 ms are 4.2 in that experiment⁵⁹, which is lower than the threshold of 6 that enables the violation of the Bell inequality². With temporal multimode DLCZ-like QMs employing REID crystal⁶⁰, Kutluer and colleagues³³ experimentally demonstrated single-mode time-bin entanglement between a SW and a photon.

With further development employing more modes in this experiment³³, multimode entanglement in time will be generated. We also note that multimode light storage with storage times well above 1 min have been demonstrated in a REID crystal⁷². Continuous-variable entanglement between light and a crystal has been generated in two temporal modes⁷³. With cold atoms, multimode SWPE generations^{58,65–69} have been experimentally demonstrated. However, the lifetimes for preserving multimode entanglement in these experiments are below 50 μ s so far. Limited to this lifetime, the entanglement between two multimode QMs linked by fibers of length longer than 10 km cannot be generated in a “heralded” way⁶⁷ (Supplementary Note 1). Thus, integrating multiplexed and long-lived qubit storages in single quantum memories remains challenging but a crucial task. For example, Pu et al.⁶⁶ demonstrated a spatially multiplexed DLCZ memory with 225 individually memory cells (modes) by dividing a cold atomic ensemble into a two-dimensional (2D) array of micro-ensembles. By storing SW modes in magnetic-field-insensitive coherence and loading the cold atoms into an optical lattice, the lifetime, which is $\sim 30 \mu$ s in that experiment⁶⁶, will be greatly prolonged. However, because of the relatively small size of the lattice-trapped atoms, the number of stored modes is strongly limiting. In a reported experiment³⁸, there are actually a large number of magnetic-field-insensitive SW modes that are along different directions around z -axis and overlap on the center of the lattice-trapped atoms. Each of these SW modes is non-classically correlated with a Stokes photon mode. By encoding these Stokes modes into multiplexed qubits, multiplexed atom–photon entanglement with long-lived lifetimes can be generated. Unfortunately, the reported scheme³⁸ to encode the memory qubit is complex and very difficult to use for multiplexing. Very recently, a spatially multiplexed DLCZ-type quantum memory generating Bell-type entanglement was demonstrated in cold atoms⁷⁴. Using a spatially resolved single-photon camera, the work achieved large-scale multimode quantum correlations between Stokes and anti-Stokes photons, with lifetimes up to 50 μ s. Yet, live feedback retrieval has not been demonstrated due to lacks of single-photon spatial routing in that work.

To overcome this key difficulty, we developed a polarization interferometer that encodes multiple Stokes modes correlated with magnetic-field-insensitive SWs into multiplexed photonic qubits. We used an ensemble of laser-cooled ⁸⁷Rb atoms as DLCZ-type memory and the approximately collinear configuration to suppress the motion-induced decoherence²³. The polarization interferometer was formed from two identical beam displacers (BDs). Three optical channels (OCs) across the polarization interferometer were built for multimode storages. The two arms of each OC, which held the H- and V-polarization modes from the BDs, were used to encode photonic qubits. The relative phase between the paired arms was passively stable^{75–78}. The atomic excitations, created by SREs, were stored as magnetic-field-insensitive SWs. We then realized a three-mode QI that preserves SWPE for 1 ms.

Results and discussion

Experimental setup and analysis. The cold atomic ensemble was centered in a polarization interferometer formed by BD1 and BD2 (see Fig. 1a). The experiment relied on SREs induced by write pulses propagating along the z -axis to create correlated pairs of Stokes photons and SW excitations. To realize the multiplexed QI (MQI), we set up three optical channels (spatial modes) that go through the polarization interferometer. The three channels (labeled $OC_{i=1,2,3}$) are arranged in a vertical plane with a separation of 4 mm. Each channel is pre-aligned with light beam. For example, the light beam in OC_i emitted from the i -th single-mode fiber at the left site (labeled

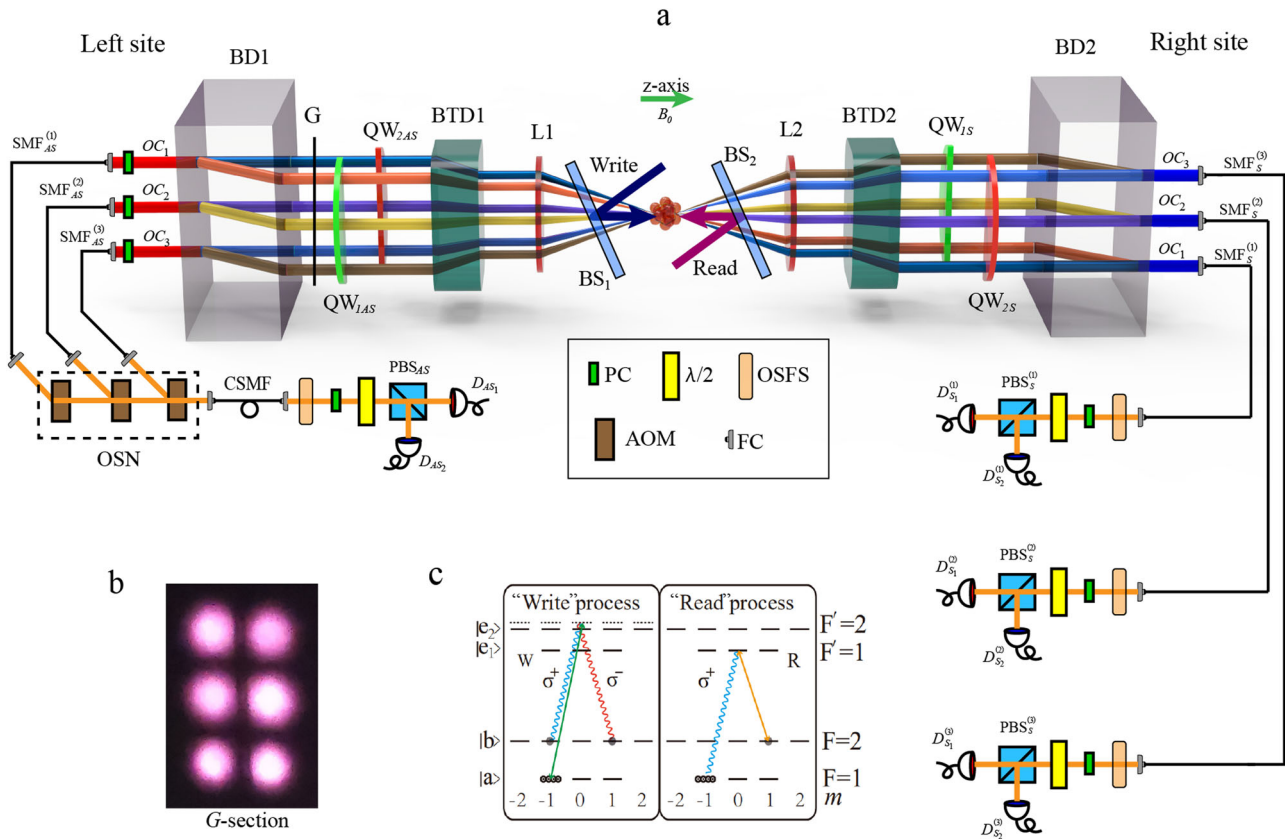


Fig. 1 Overview of the experiment. **a** Experiment setup for the three-mode MQI (multiplexed quantum interface). PC: phase compensator (“Methods” section); CSMF: common single-mode fiber; OSN: optical switching network; QW: $\lambda/4$ wave-plate; BD: beam displacer, PBS: polarization-beam splitter; BTD: beam transformation device; SMF: single-mode fiber; OC: optical channel. BS₁ (BS₂): Non-polarizing beam splitter, whose reflectance (transmission) is 10% (90%). The write beam is aligned along the z-axis via BS₁, and the read beam along the opposite direction to that of the write beam via BS₂; AOM: acoustic-optic modulator; FC: fiber coupler; OSFS: optical-spectrum-filter set (“Methods” section). B₀: bias magnetic field (4G). **b** Pattern of the array at the G-section. **c** Relevant atomic levels.

by $SMF_{AS}^{(i)}$ enters BD1, which splits the H (horizontally)- and V (vertically)-polarized components of the beam into two arms (spatial modes) of the polarization interferometer. The two spatial modes are denoted by $A_L^{(i)}$ and $A_R^{(i)}$, respectively; here, “A” denotes the arm, subscripts L and R distinguish the two modes, and superscript i denotes the i -th OC for the two modes. The use of L and R as subscripts is based on the following fact that the two modes pass through the G-section on the left and at the right, respectively (see Fig. 1b). Exiting from BD1, the two components of the beam parallel propagate in a horizontal plane, with the same separation of 4 mm. Hence, there are six spatial modes ($A_\alpha^{(i)}$ with $\alpha = R, L; i = 1$ to 3), which are arranged in parallel in a two-dimensional array (G-section of the array in Fig. 1b). The optical elements (Fig. 1a) including two identical lenses (L1 and L2) and two beam transformation devices (BTD1 and BTD2), are inserted in the polarization interferometer, where BTD1 (BTD2) is formed by two lenses, which shrink (expand) the beam array by factor F_{BTD} (“Methods” section). The effective multimode storages rely on strong couplings of the Stokes and retrieved photons with the atoms. To this end, we use lens L1 to focus the six modes at the center of the atoms. To ensure the multimode storages have long lifetimes, we have to store long-wavelength SWs, which in turn require the angles $\vartheta_{A_\alpha}^{(i)}$ of the six modes $A_\alpha^{(i)}$ relative to the write beam (z-axis) to be reduced to very small values^{23,79}. The angles are calculated from $\vartheta_{A_\alpha}^{(i)} = \left(\sqrt{4(i-2)^2 + 1}\right) B_f / 2f$ (Supplementary Note 2), where B_f denotes the beam separation of the array on lens L1, and f the focal length of L1. To reduce the values of

the angles significantly, we selected $f = 1.425\text{m}$ and used BTD1 to reduce the array beam separation by factor $F_{BTD} = 2$. After BTD1, the array propagates parallel to L1 and has a separation of $B_f \approx 2\text{ mm}$. We then obtain small angles $\{\vartheta_{A_R}^{(1)} = \vartheta_{A_L}^{(1)} \approx 0.09^\circ, \vartheta_{A_R}^{(2)} = \vartheta_{A_L}^{(2)} \approx 0.04^\circ, \vartheta_{A_R}^{(3)} = \vartheta_{A_L}^{(3)} \approx 0.09^\circ\}$, which correspond to lifetimes limited by the atomic motion of $\{840\ \mu\text{s}, 1850\ \mu\text{s}, 840\ \mu\text{s}\}$ for modes $\{A_{R,L}^{(1)}, A_{R,L}^{(2)}, A_{R,L}^{(3)}\}$, respectively (Supplementary Note 3). Additionally, the $1/e$ spot size of each array mode at the atomic center is 0.55 mm, which is much less than the atomic transverse size (2 mm). After passing through the atoms, the six crossed beams are transformed to a parallel beam array by L2. Then, the array goes through BTD2 and is expanded by factor $F_{BTD} = 2$. After the transformation, this array has the same beam separations and sizes (see Fig. 1b). Next, the array passes through BD2, which combines the paired arm modes into single spatial modes; for example, $A_R^{(i)}$ and $A_L^{(i)}$ modes are combined into single light beam in OC _{i} . Finally, with high efficiency (“Methods” section), the light beam in OC _{i} is coupled to the i -th single-mode fiber on the right site (labeled $SMF_S^{(i)}$ in Fig. 1a).

The relevant Rb atomic levels (Fig. 1c) are $|a\rangle = |5^2S_{1/2}, F=1\rangle$, $|b\rangle = |5^2S_{1/2}, F=2\rangle$, $|e_1\rangle = |5^2P_{1/2}, F'=1\rangle$, and $|e_2\rangle = |5^2P_{1/2}, F'=2\rangle$. After the atoms are prepared in the Zeeman state $|a, m_a = -1\rangle$ via optical pumping⁸⁰, we start the SWPE generation (“Methods” section). At the beginning of a trail, a write pulse of 20 MHz blue-detuned to the $|a\rangle \rightarrow |e_2\rangle$ transition

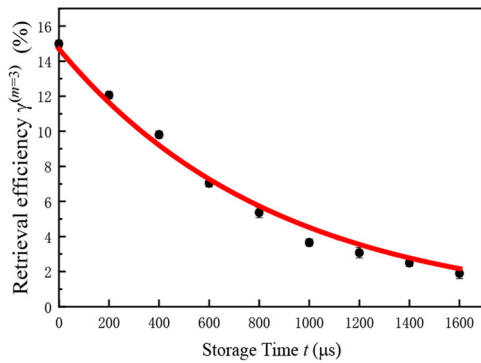


Fig. 2 Retrieval efficiency of the multiplexed QM (quantum memory) as a function of t . Black circles are the experimental data of the measured retrieval efficiency of the MQI (multiplexed quantum interface) based on storages of the three SW (spin wave) qubits. Red line is the linear best fits of the experimental data based on $\gamma^{(m=3)}(t) = \gamma_0 e^{-t/\tau_0}$. The errors associated with the data correspond to one standard deviation of the measured value and are smaller than the data points displayed.

is applied to the atoms. This write pulse induces the Raman transition $|a, m_a = -1\rangle \rightarrow |b, m_b = 1\rangle$ ($|a, m_a = -1\rangle \rightarrow |b, m_b = -1\rangle$) via $|e_2, m' = 0\rangle$, which may emit σ^- -polarized (σ^+ -polarized) Stokes photons and create simultaneously SW excitations associated with the coherence $|m_a = -1\rangle \leftrightarrow |m_b = 1\rangle$ ($|m_a = -1\rangle \leftrightarrow |m_b = -1\rangle$) (Fig. 1c), where $|m_a = -1\rangle \leftrightarrow |m_b = 1\rangle$ and $|m_a = -1\rangle \leftrightarrow |m_b = -1\rangle$ are the magnetic-field-insensitive and the magnetic-field-sensitive coherences, respectively. A Stokes photon coupled to the $A_R^{(i)}$ ($A_L^{(i)}$) mode and moving towards the right is denoted by $S_R^{(i)}$ ($S_L^{(i)}$). In this case, one excitation is created in the SW mode $M_R^{(i)}$ ($M_L^{(i)}$) defined by the wave-vector $\mathbf{k}_{M_R}^{(i)} = \mathbf{k}_w - \mathbf{k}_{S_R}^{(i)}$ ($\mathbf{k}_{M_L}^{(i)} = \mathbf{k}_w - \mathbf{k}_{S_L}^{(i)}$), where \mathbf{k}_w denotes the wave-vector of the write pulse, and $\mathbf{k}_{S_R}^{(i)}$ ($\mathbf{k}_{S_L}^{(i)}$) that of the Stokes photon $S_R^{(i)}$ ($S_L^{(i)}$). In Fig. 1a, the σ^- -polarized $S_R^{(i)}$ ($S_L^{(i)}$) photons are transformed into H (V)-polarized photons by the $\lambda/4$ plate labeled QW_{1S} (QW_{2S}). After BD2, the H (V)-polarized $S_R^{(i)}$ and $S_L^{(i)}$ modes are combined to form a Stokes qubit $S^{(i)}$ and then are coupled to $SMF_S^{(i)}$. In addition, the corresponding excitations in the $M_R^{(i)}$ and $M_L^{(i)}$ modes are stored as magnetic-field-insensitive SWs, which represent the i -th atomic qubit. In a single channel, for example, in the i -th channel, the joint state of the atom-photon system may be written as³¹

$\rho_{ap}^{i-\text{th}} = |0\rangle\langle 0| + \chi_i |\Phi_{a-p}^{i-\text{th}}\rangle\langle \Phi_{a-p}^{i-\text{th}}|$, where $|0\rangle$ denotes the vacuum, $\chi_i (\ll 1)$ represents the probability of creating the $|\Phi_{a-p}^{i-\text{th}}\rangle$ state in each trial, $\Phi_{a-p}^{i-\text{th}} = |H\rangle_S^{(i)} |M_R\rangle_{\text{MFI}}^{(i)} + e^{i\varphi_i} |V\rangle_S^{(i)} |M_L\rangle_{\text{MFI}}^{(i)}$ denotes entanglement between the i -th atomic and photonic qubits. Here, $|H\rangle_S^{(i)}$ ($|V\rangle_S^{(i)}$) denotes the H (V)-polarized Stokes photon of the qubit $S^{(i)}$, $|M_R\rangle_{\text{MFI}}^{(i)}$ ($|M_L\rangle_{\text{MFI}}^{(i)}$) a single SW excitation associated with the magnetic-field-insensitive (MFI) coherence and stored in the modes $M_R^{(i)}$ ($M_L^{(i)}$), and φ_i the phase difference between the $S_R^{(i)}$ and $S_L^{(i)}$ fields. If the $S_R^{(i)}$ ($S_L^{(i)}$) photon is σ^+ -polarized, the corresponding excitation in the $M_R^{(i)}$ ($M_L^{(i)}$) mode is stored as the magnetic-field-sensitive SW and decays rapidly⁸¹. However, these photons are abandoned because they are excluded from collections (“Methods” section).

Returning to the entangled state $\Phi_{a-p}^{i-\text{th}}$, the qubit $S^{(i)}$ is guided into the i -th polarization-beam splitter ($PBS_S^{(i)}$) after the $SMF_S^{(i)}$. The two outputs of the $PBS_S^{(i)}$ are sent to single-photon detectors

$D_{S_1}^{(i)}$ and $D_{S_2}^{(i)}$. The polarization angle of qubit $S^{(i)}$, denoted by $\theta_S^{(i)}$ may be changed by rotating the $\lambda/2$ -plate before the $PBS_S^{(i)}$. Here, we set $\theta_S^{(1)} = \theta_S^{(2)} = \theta_S^{(3)} = \theta_S$. Once a photon is detected by $D_{S_R}^{(i)}$ ($D_{S_L}^{(i)}$), a magnetic-field-insensitive excitation, which is stored in the mode $M_R^{(i)}$ or $M_L^{(i)}$ ($M_R^{(i)}$ or $M_L^{(i)}$), is heralded. After a storage time t , we apply a read pulse that counter-propagates with the write beam to convert the magnetic-field-insensitive SW excitation $|M_R\rangle^{(i)}$ ($|M_L\rangle^{(i)}$) into an anti-Stokes photon $AS_R^{(i)}$ ($AS_L^{(i)}$). The retrieved photon $AS_R^{(i)}$ ($AS_L^{(i)}$) is emitted into the spatial mode determined by the wave-vector constraint $\mathbf{k}_{AS_R}^{(i)} \approx -\mathbf{k}_{S_R}^{(i)}$ ($\mathbf{k}_{AS_L}^{(i)} \approx -\mathbf{k}_{S_L}^{(i)}$); i.e., it propagates in arm $A_R^{(i)}$ ($A_L^{(i)}$) in the opposite direction to the $S_R^{(i)}$ ($S_L^{(i)}$) photon. The $AS_R^{(i)}$ ($AS_L^{(i)}$) photon is σ^+ -polarized and transformed into the H (V)-polarized photon by a $\lambda/4$ plate labeled QW_{1AS} (QW_{2AS}). After BD1, the $AS_R^{(i)}$ and $AS_L^{(i)}$ fields are combined to form a polarization qubit ($AS^{(i)}$). Thus, the atom-photon state $\Phi_{a-p}^{i-\text{th}}$ is transformed into the two-photon entangled state, $\Phi_{pp}^{i-\text{th}} = |H\rangle_S^{(i)} |H\rangle_{AS}^{(i)} + e^{i(\varphi_i + \psi_i)} |V\rangle_S^{(i)} |V\rangle_{AS}^{(i)}$, where ψ_i denotes the phase difference between the anti-Stokes fields in arms $A_R^{(i)}$ and $A_L^{(i)}$ before they overlap at BD1. Using the phase compensator in the OC_i (see left site of Fig. 1), we set the phase difference $\varphi_i + \psi_i$ to zero. We next describe how the spin waves in our experiment are independently stored, i.e., the orthogonality of the two adjacent spin-wave modes, that enables us to avoid entanglement degradations arising from cross talk between the adjacent spin waves. As pointed out in a previous paper⁸², independent storage requires the angular separation θ_d of adjacent spin-wave modes to be of order $\sim \lambda/w$, where $\lambda(w)$ is the wavelength (spot size) of the Stokes (anti-Stokes) modes. The actual angular separation in our experiment is $>0.08^\circ$, i.e., 1.4×10^{-3} (Supplementary note 2), which is in agreement with the calculated result of $\theta_d = \lambda/w \approx 1.4 \times 10^{-3}$ using $\lambda = 795\text{nm}$ and $w \approx 550\ \mu\text{m}$. Therefore, the adjacent spin-wave states (e.g., $M_R^{(i)}$ and $M_L^{(i)}$ or $M_R^{(i+1)}$ states) are orthogonal in our experiment. The generation of atom-photon (photon-photon) entanglement using $m = 3$ storage modes, constitutes the MQI. To enable the MQI to be available for the multiplexed QR scheme⁵⁸, we introduced an optical switch network (OSN), which routes the retrieved photons into a specific mode (common single-mode fiber). Passing through this fiber and a $\lambda/2$ -plate, the qubits $AS^{(i)}$ ($i = 1$ to 3) impinge on a polarization-beam splitter, PBS_{AS} .

Experimental results. To show that the MQI provides long-lived SW storage, we examined the dependence of retrieval efficiency on the storage time t . The retrieval efficiency of the m -mode MQI is measured as $\gamma^{(m)} = \sum_{i=1}^m P_{S,AS}^{i-\text{th}} / (\eta_{AS} \sum_{i=1}^m P_S^{i-\text{th}})$, where η_{AS} denotes the detection efficiency in the anti-Stokes channel, $P_{S,AS}^{i-\text{th}} = P_{D_{S_1}, D_{AS_1}}^{i-\text{th}} + P_{D_{S_2}, D_{AS_2}}^{i-\text{th}}$ the Stokes-anti-Stokes coincidence probability, $P_{D_{S_1}, D_{AS_1}}^{i-\text{th}}$ ($P_{D_{S_2}, D_{AS_2}}^{i-\text{th}}$) the probability of detecting a coincidence between the detectors $D_{S_1}^{(i)}$ ($D_{S_2}^{(i)}$) and D_{AS_1} (D_{AS_2}), $P_S^{i-\text{th}} = P_{D_{S_1}}^{i-\text{th}} + P_{D_{S_2}}^{i-\text{th}}$ the Stokes-detection probability, and $P_{D_{S_1}}^{i-\text{th}}$ ($P_{D_{S_2}}^{i-\text{th}}$) the probability of detecting a photon at $D_{S_1}^{(i)}$ ($D_{S_2}^{(i)}$). Both $P_{S,AS}^{i-\text{th}}$ and $P_S^{i-\text{th}}$ are measured for $\theta_S = \theta_{AS} = 0^\circ$, and θ_{AS} is the polarization angle of the $AS^{(i)}$ qubits, which is set by the $\lambda/2$ plate before PBS_{AS} . The measured retrieval efficiency of the MQI based on storages of the three SW qubits are shown in Fig. 2 (black circles). The fitting function (solid red curve) based on $\gamma^{(m=3)}(t) = \gamma_0 e^{-t/\tau_0}$ yields a zero-delay retrieval efficiency

$\gamma_0 \approx 15\%$ and $1/e$ storage time $\tau_0 \approx 870 \mu\text{s}$. This lifetime is consistent with the average lifetime over the three SW qubits (Supplementary note 4). The double excitations lead to errors in the Stokes–anti-Stokes coincidences in a write trial². To avoid double excitations, we kept the excitation probabilities χ_i ($i = 1$ to 3) to a low level, which is achieved by manipulating the write laser pulse. We evaluated the value of the excitation probability χ_i from the Stokes-photon generation rate $C_S^{i\text{-th}} = rP_S^{i\text{-th}} = r\chi_i\eta_S^{i\text{-th}}$, where $r = 8 \times 10^4$ is the repetition rate for storage time $t = 1 \mu\text{s}$ (see “Methods” section for details), and $\eta_S^{i\text{-th}}$ is the detection efficiency of the i -th Stokes channel. In the experiment described, the detection efficiencies for the 1-st, 2-nd, and 3-rd channels are approximately identical, i.e., $\eta_S^{1\text{-th}} \approx \eta_S^{2\text{-th}} \approx \eta_S^{3\text{-th}} = \eta_S \approx 0.19$. The measured Stokes-photon generation rates of the three channels are all $\sim 150\text{s}^{-1}$. With these data, we evaluated the Stokes detection probabilities $P_S^{1\text{-th}} \approx P_S^{2\text{-th}} \approx P_S^{3\text{-th}} \approx P_S \approx 1.9 \times 10^{-3}$ and the excitation probabilities $\chi_1 \approx \chi_2 \approx \chi_3 \approx \chi \approx 0.01$. In addition, the detected anti-Stokes-photon generation rate C_{AS} for each channel is $\sim 84\text{s}^{-1}$. Using $C_{AS} = rP_{AS}$, we obtained the anti-Stokes-photon probability $P_{AS} \approx 1 \times 10^{-3}$. The probability of detecting a coincidence between the Stokes and anti-Stokes detectors is $P_{S,AS} \approx 5 \times 10^{-5}$ for each channel. The quantum correlation $g^{(2)}$ between the Stokes and anti-Stokes photons can be calculated using the relation² $g^{(2)} = P_{S,AS}/P_S P_{AS}$

and yields $g^{(2)} \approx 26$. Decreasing the excitation probability χ further increases significantly the quantum correlation $g^{(2)}$ ^{19,83,84}.

The quality of the m -mode SWPE described by the Clauser–Horne–Shimony–Holt Bell parameter $S^{(m)}$ ⁵⁸ is written

$$S^{(m)} = |E^{(m)}(\theta_S, \theta_{AS}) - E^{(m)}(\theta_S, \theta'_{AS}) + E^{(m)}(\theta'_S, \theta_{AS}) + E^{(m)}(\theta'_S, \theta'_{AS})| < 2 \quad (1)$$

with the correlation function $E^{(m)}(\theta_S, \theta_{AS})$ defined by

$$\frac{\sum_{i=1}^m [C_{D_{S_1}, D_{AS_1}}^{i\text{-th}}(\theta_S, \theta_{AS}) + C_{D_{S_2}, D_{AS_2}}^{i\text{-th}}(\theta_S, \theta_{AS}) - C_{D_{S_1}, D_{AS_2}}^{i\text{-th}}(\theta_S, \theta_{AS}) - C_{D_{S_2}, D_{AS_1}}^{i\text{-th}}(\theta_S, \theta_{AS})]}{\sum_{i=1}^m [C_{D_{S_1}, D_{AS_1}}^{i\text{-th}}(\theta_S, \theta_{AS}) + C_{D_{S_2}, D_{AS_2}}^{i\text{-th}}(\theta_S, \theta_{AS}) + C_{D_{S_1}, D_{AS_2}}^{i\text{-th}}(\theta_S, \theta_{AS}) + C_{D_{S_2}, D_{AS_1}}^{i\text{-th}}(\theta_S, \theta_{AS})]} \quad (2)$$

where, for example, $C_{D_{S_1}, D_{AS_1}}^{i\text{-th}}(\theta_S, \theta_{AS})$ ($C_{D_{S_2}, D_{AS_2}}^{i\text{-th}}(\theta_S, \theta_{AS})$) denotes the coincidence counts between detectors $D_{S_1}^{(i)}$ ($D_{S_2}^{(i)}$) and D_{AS_1} (D_{AS_2}) for the polarization angles θ_S and θ_{AS} . In the $S^{(m)}$ measurement, we used the canonical settings $\theta_S = 0^\circ$, $\theta'_S = 45^\circ$, $\theta_{AS} = 22.5^\circ$, and $\theta'_{AS} = 67.5^\circ$. To demonstrate that our three-mode MQI preserves entanglement over a long duration, we measured the decay of the parameter $S^{(m=3)}$ for various storage times t (blue squares in Fig. 3). At $t = 1$ ms, $S^{(m=3)} = 2.07 \pm 0.02$, which violates the Bell inequality by 3.5 standard deviations.

The quality of the photon–photon (atom–photon) entanglement generated from the m -mode MQI can also be characterized by the fidelity, given by $F^{(m)} = \text{Tr} \left(\sqrt{\sqrt{\rho_r^{(m)}} \rho_d \sqrt{\rho_r^{(m)}}} \right)^2$, where

$\rho_r^{(m)}$ (ρ_d) denotes the reconstructed (ideal) density matrix of the two-photon entangled state. From measurements of the Stokes–anti-Stokes coincidences for $t = 1 \mu\text{s}$ and $\chi = 1\%$, we reconstructed $\rho_r^{(m=3)}$ (Supplementary Note 6), which yields $F^{(m=3)} = 90.4 \pm 1.6\%$. We also reconstructed the density matrices $\rho_r^{i\text{-th}}$ of the entangled states $\Phi_{pp}^{i\text{-th}}$, which yields fidelities $F^{(1\text{-th})} = 88.6 \pm 1.13\%$, $F^{(2\text{-th})} = 92.0 \pm 1.5\%$, and $F^{(3\text{-th})} = 88.4 \pm 0.85\%$ (Supplementary Note 6).

For a multiplexed atom–photon entanglement interface, demonstrating that, compared with the non-multiplexed interface, this interface has the capacity to enhance the probability of generating entangled atom–photon (photon–photon) pairs is important. The probability of generating an atom–photon (photon–photon) entangled pair corresponds to the total Stokes detection (Stokes–anti-Stokes coincidence) probability

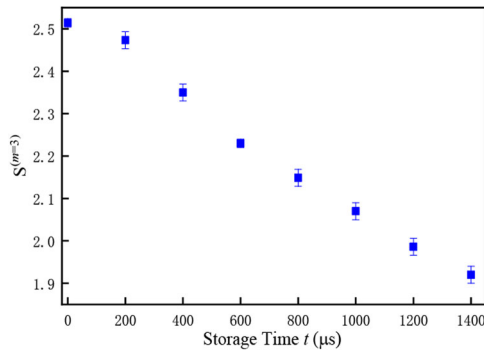


Fig. 3 Bell parameters $S^{(m)}$ as a function of t for $\chi = 1\%$. Blue squares are experimental data of the decay of the parameter $S^{(m=3)}$ for various storage times t . The error bars represent the standard deviation of measured values.

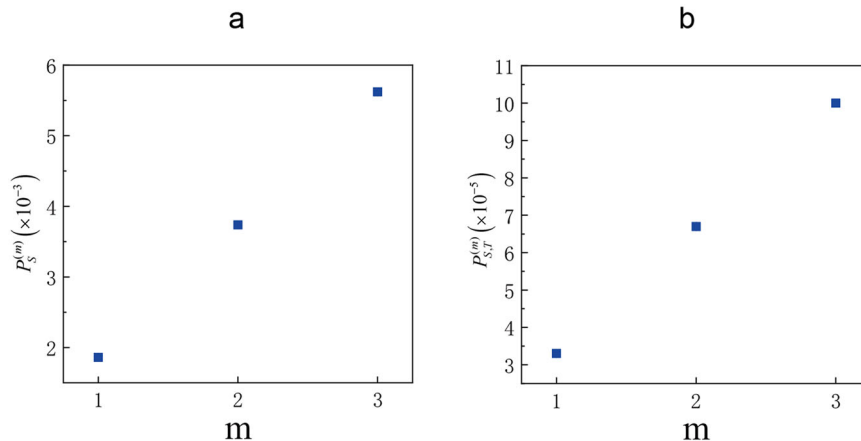


Fig. 4 Stokes detection probability and Stokes–anti-Stokes coincidence probability. **a** Blue squares are the measured values of Stokes detection probability $P_S^{(m)}$ as a function of the number of modes m . **b** Blue squares are the measured values of Stokes–anti-Stokes coincidence probability $P_{S,AS}^{(m)}$ as a function of the number of modes m . The errors associated with the data correspond to one standard deviation of the measured value and are smaller than the data points displayed.

$P_S^{(m)} = \sum_{i=1}^m P_S^{i\text{-th}}$ ($P_{S,AS}^{(m)} = \sum_{i=1}^m P_{S,AS}^{i\text{-th}}$). The blue squares in Fig. 4a (Fig. 4b) are the measured values of $P_S^{(m)}$ ($P_{S,AS}^{(m)}$) as a function of m and show that the MQI gives rise to a threefold increase in the atom-photon (photon-photon) entanglement-generation probability compared with single-mode QIs. The average OSN efficiency is written as $\eta_{\text{OSN}} = \Gamma_A(1 - (m-1)\Upsilon_A/2)$ (“Methods” section), where Γ_A denotes the diffraction efficiency of the acousto-optic modulator, and Υ_A the transmission loss for the case that modulator is not driven. For our experiment, $\Gamma_A \approx 82\%$ and $\Upsilon_A \approx 0.02$ is small; with $m=3$, we have $\eta_{\text{OSN}} \approx 0.8$. Considering the efficiency of OSN, the MQI increases this probability by a factor of $m \times \eta_{\text{SW}} = 2.4$ compared with the single-mode QI without OSN. In our experiment, the limitation in scaling up to more than three modes is because transverse sizes of the optical elements are small, specifically, beam displacers in the polarization interferometer. When the transverse sizes of the beam displacers and other optical elements are increased, the mode number may be scaled up. For example, when the transverse sizes of the optical elements are increased to $26 \times 24 \text{ mm}^2$, the number of stored qubits (modes) may be extended to 12. With an increased mode number, the larger angles between the z -axis (write beam direction) and the Stokes fields lead to decreases in lifetimes. The evaluated average lifetime of 12 storage modes is about $510 \mu\text{s}$. However, this decrease is not a fundamental limitation and may be overcome by trapping the atoms in an optical lattice.

Conclusion

The current work exploited the spatially multiplexed correlations between Stokes photon and SWs and the feed-forward controlled retrieval, which were used in our previous work⁵⁸, to achieve a threefold increase in the generation rate of Stokes-anti-Stokes pairs, compared with the non-multiplexed case. In contrast to the previous work, in which each memory qubit is stored as two spin waves with one being associated with the magnetic-field-insensitive Zeeman coherence and the another with magnetic-field-sensitive coherence, the current work used a polarization interferometer to encode multiplexed photonic qubits onto multiple Stokes modes that are only correlated with magnetic-field insensitive SWs of long wavelength. Therefore, the entanglement storage lifetimes reach up to 1 ms, which is 20 times higher than our previous result of $50 \mu\text{s}$ ⁵⁸. However, to apply the present MQI in QR applications, its performance needs to be improved. Millisecond lifetimes are mainly limited by motional dephasing (Supplementary Note 5) but can be prolonged to 0.2 s by trapping the atoms in an optical lattice^{26,27}. In the experiment described, the number of modes is six, which can be increased by extending the apertures of the optical devices. The multimode number may be extended using multiplexing schemes with two degrees of freedom, e.g., combining a temporal multiplexing scheme⁶⁸ with the present spatial approach. Considering an MQI that stores 12 spatial and 10 temporal SW qubits, the total number of memory qubits is $N_m = 120$. To minimize transmission losses in fibers, the Stokes photons (795 nm) has to be converted into photons in the telecommunications band^{49,85–87}. The lower retrieval efficiency (15%) can be increased using high optical-depth cold atoms^{75,76,88,89} or coupling the atoms with an optical cavity^{24,39} to enhance the collective interference (Supplementary Note 7). The measured average entanglement fidelity of the three channels is $\sim 90\%$. We attributed the 10% decrease in entanglement fidelity to imperfect phase compensations of the OSN and the relatively low-quantum correlations ($g^{(2)} \approx 26$) between the Stokes and anti-Stokes photons (Supplementary Note 8). In future work, we need to enhance the entanglement

fidelity by improving phase compensations of the OSN and increasing $g^{(2)}$ (ref. 31). Our present experiment shows a promising way to store multiplexed memory qubits as magnetic-field-insensitive SWs, thereby allowing a realization of an entanglement QI capable of storing a large number of long-lived memory qubits in lattice-trapped atoms. Such capabilities would be of benefit in QR-based long-distance quantum communications.

Methods

Experimental method. The experiment is performed in cycles. In each cycle, the duration for the preparation of cold atoms and that for the experimental run of the SWPE generation are 42 ms and 8 ms, respectively, corresponding to a 20-Hz cycle frequency. During preparations, $>10^8$ atoms of ^{87}Rb are trapped in a two-dimension magneto-optical trap (MOT) for 41.5 ms and further cooled by Sisyphus cooling for 0.5 ms. The cloud of cold atoms has a size of $\sim 5 \times 2 \times 2 \text{ mm}^3$, a temperature of $\sim 100 \mu\text{K}$ and an optical density of about 14. At the end of each preparation stage, a bias magnetic field of $B_0 = 4 \text{ G}$ is applied along the z -axis (see Fig. 1a) and the atoms are prepared into the initial level $|5^2S_{1/2}, F=1, m=-1\rangle$ via optical pumping⁷⁹. After the preparation stage, the 8-ms experimental run containing a large number of SWPE-generation trials starts. At the beginning of a trial, a write pulse of 70 ns duration is applied on the atomic ensemble to generate correlated pairs of Stokes photons and SW excitations. The detection events at the Stokes detectors $D_S^{(i=1,2,3)}$ (i.e., $D_S^{(i=1,2,3)}$) and $D_{S_2}^{(i=1,2,3)}$ in Fig. 1a) are analyzed using a field programmable gate array (FPGA). As soon as a Stokes photon qubit is detected by any of these detectors, for example, $D_S^{(i)}$ ($D_S^{(i)}$ or $D_{S_2}^{(i)}$), the atom-photon entanglement is generated in the i -th channel and the FPGA sends out a feed-forward signal to stop the write processes. After a storage time t , a read laser pulse of 70 ns duration is applied to the atoms to convert the SW qubit into an anti-Stokes photon qubit $AS^{(i)}$. At the same time, the FPGA delivers a feed-forward signal to switch the optical switching network (OSN) and then the anti-Stokes photon qubit is routed into the common single-mode fiber (CSMF)⁵⁸. After a 1300 ns interval, a cleaning pulse of 200 ns duration is applied to pump the atoms into the initial level $|5^2S_{1/2}, F=1, m=-1\rangle$. Then, the next SWPE-generation trial starts. If no Stokes photon is detected during the write pulse, the atoms are pumped directly back into the initial level by the read and cleaning pulses for the subsequent trial to start. The delay between the two adjacent write pulses for a storage time $t \approx 1 \mu\text{s}$ is 2000 ns. Therefore, the 8 ms experimental run contains ~ 4000 experimental trials. Considering that 1-s experiment contains 20 cycles, the repetition rate of the SWPE-generation trial is $r = 8 \times 10^4$.

In the center of the atoms, the diameters of the write and read light beams are both $\sim 1.1 \text{ mm}$; however, the power of the beams are $\sim 100 \mu\text{W}$ and $\sim 1 \text{ mW}$, respectively. The read light field is on resonance with transition $|b\rangle \rightarrow |e_1\rangle$. At the right site in Fig. 1a, the BD2 perfectly combines both $A_R^{(i)}$ (H -polarization) and $A_L^{(i)}$ (V -polarization) modes into a single light beam propagating in channel OC₂ and then the light beam is effectively coupled into the single-mode fiber SMF_S⁽ⁱ⁾. The measured coupling efficiencies for modes $\{A_R^{(1)}, A_L^{(1)}\}$, $\{A_R^{(2)}, A_L^{(2)}\}$, and $\{A_R^{(3)}, A_L^{(3)}\}$ are {70.5%, 71.0%}, {70.6%, 71.5%}, and {70.8%, 70%}, respectively. For blocking the write (read) beam in the Stokes and anti-Stokes channels, we placed an optical-spectrum-filter set (OSFS) before each polarization-beam splitter (PBS). Each OSFS comprises four Fabry-Pérot etalons, which attenuate the write (read) beam by factor $\sim 2.7 \times 10^{-9}$ ($\sim 3.7 \times 10^{-9}$) and transmit the Stokes ((anti-Stokes) fields with a transmission efficiency of $\sim 65\%$. Additionally, in the Stokes (anti-Stokes) detection channel, the spatial separation of the Stokes (anti-Stokes) fields from the strong write (read) beam provides an attenuation of $\sim 10^{-4}$ for the write (read) beam. In the present experiment, we measured the uncorrelated noise probability in the anti-Stokes mode, which is $p_n = 9 \times 10^{-5}$ per read pulse (70 ns). This noise mainly results from the leakage of the read beam into the anti-Stokes detection channel.

From the SRE induced by the write pulse, if the Stokes photon $S_R^{(i)}$ ($S_L^{(i)}$) is σ^+ -polarization, it is transformed into a V (H)-polarized photon by the $\lambda/4$ waveplate QW_{1S} (QW_{2S}) (see Fig. 1a) and then removed from OC₂ by BD2.

The total detection efficiency for detecting the Stokes photons at the detector D_{S_1} (D_{S_2}), denoted by η_S , includes the transmission of the BS2 ($\eta_{\text{BS}} = 90\%$), the coupling efficiency of the single-mode fiber SMF_{S} $\sim 70.7\%$, the transmission of $\sim 65\%$ for the OSFS, the transmission of a multimode fiber (MMF) $\eta_{\text{MMF}} = 92\%$, and the quantum efficiency 0.5 of the detector D_{S_1} (D_{S_2}), respectively. The overall detection efficiency is $\eta_S = \eta_{\text{BS}} \times \eta_{\text{SMF}_S} \times \eta_{\text{MMF}} \times \eta_D \approx 19\%$.}

Similarly, the total detection efficiency for detecting the anti-Stokes photons at the detector D_{AS_1} (D_{AS_2}), denoted by η_{AS} , includes the transmissions of the BS1 ($\eta_{\text{BS}} = 90\%$), the coupling efficiency $\sim 70.7\%$ of the single-mode fiber SMF_{AS}, the optical switching network (OSN) efficiency of 80%, the coupling efficiency of the CSMF ($\eta_{\text{CSMF}} = 80\%$), the transmission of the OSFS $\eta_{\text{OSFS}} = 65\%$, and the}

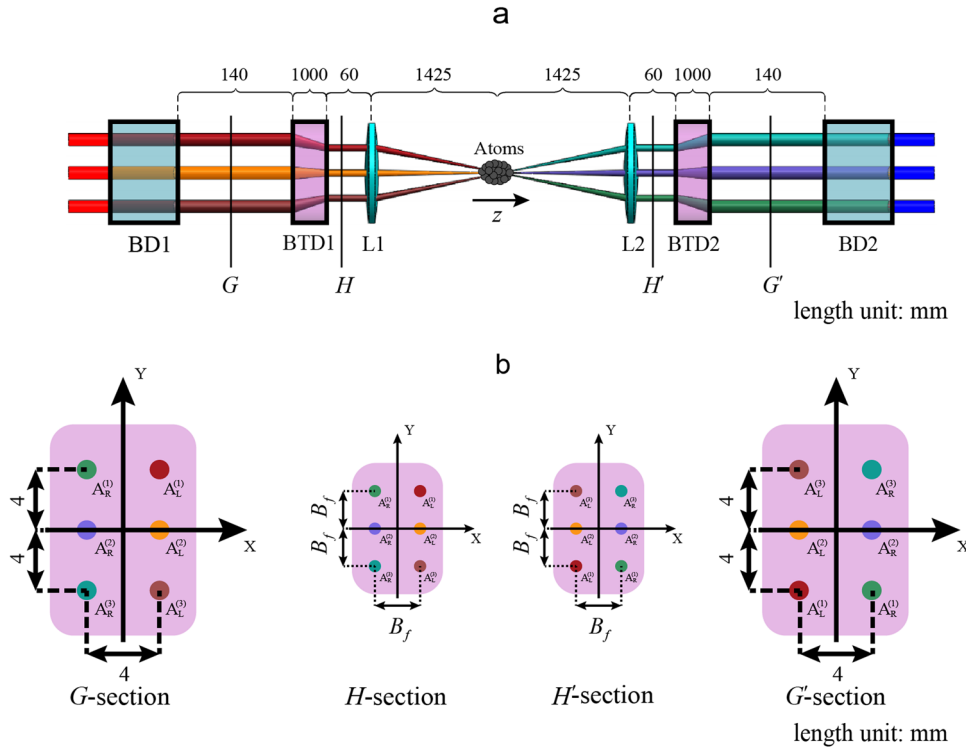


Fig. 5 Configuration of the PI (polarization interferometer) and cross sections of the array at different sites. a Configuration of the PI. **b** Cross section of the array at G, H, H', and G' sites, where $B_f = 2$ mm.

transmission of the MMF $\eta_{MMF} = 92\%$, the quantum efficiency 0.5 of the detector $D_{AS_1}(D_{AS_2})$, respectively. The total detection efficiency is $\eta_{AS} = \eta_{BS} \times \eta_{SMF_{AS}} \times \eta_{OSN} \times \eta_{CSMF} \times \eta_{OSFS} \times \eta_{MMF} \times \eta_D \approx 12\%$.

All error bars in the experimental data represent $a \pm 1$ standard deviation, which is estimated from the Poissonian detection statistics using Monte Carlo simulations.

Propagating directions of the retrieved photons. Because of the collective interference of atoms, the retrieved photon $AS_L^{(i)}(AS_R^{(i)})$ is emitted into a well-defined spatial mode given by the phase matching condition, $\mathbf{k}_{AS_R}^{(i)} = \mathbf{k}_{M_R}^{(i)} + \mathbf{k}_r = \mathbf{k}_w - \mathbf{k}_R^{(i)} + \mathbf{k}_r$ ($\mathbf{k}_{AS_L}^{(i)} = \mathbf{k}_{M_L}^{(i)} + \mathbf{k}_r = \mathbf{k}_w - \mathbf{k}_{S_L}^{(i)} + \mathbf{k}_r$), where \mathbf{k}_r (\mathbf{k}_w) is the wave-vector of the read (write) beam. As the write and read light beams counter-propagate through the atoms, we have $\mathbf{k}_r \approx -\mathbf{k}_w$ and hence $\mathbf{k}_{AS_R}^{(i)} \approx -\mathbf{k}_{S_R}^{(i)}$ ($\mathbf{k}_{AS_L}^{(i)} \approx -\mathbf{k}_{S_L}^{(i)}$).

Phase compensators (PCs). When the H- and V-polarized light fields propagate in the two paired arms in the BDs, the difference in the refractive indices of the two arms leads to a phase shift between the two light fields. We use PCs to overcome this problem. For example, to eliminate the phase shift due to the BDs in the i -th channel (OC_i), we place the phase compensator PC_i between BD1 and the i -th single-mode fiber at the left site. Each phase compensator is a combination of the $\lambda/4$, $\lambda/2$, and $\lambda/4$ wave-plates⁵⁸. By rotating the $\lambda/2$ wave-plate in the PC_i , we eliminate the phase shift caused by the BDs ($\varphi_i + \psi_i$). We also insert a PC before each PBS (see Fig. 1a) to eliminate phase shifts caused by optical elements such as the single-mode fibers and acoustic-optical modulators (AOMs).

Optical switching network. The optical switching network is composed of m AOMs, which are placed in a straight line. To understand the optical circuit of OSN, Fig. 1a shows a network with three AOMs. The i -th AOM is used to route the retrieved photon from the i -th channel into the line. Then, the photon goes through $(m-i)$ AOMs that do not work and is coupled to the CSMF. The OSN efficiency of the i -th channel, which corresponds to the transmission of the photon from i -th channel to the fore of the CSMF, is $\eta_{OSN}^{i-th} = \Gamma_A (1 - \Upsilon_A)^{m-i}$, where Γ_A is the diffraction efficiency of the AOM, and Υ_A the transmission loss for the case that modulator is not driven. For a small Υ_A , the OSN transmission efficiency for the i -th channel is written $\eta_{OSN}^{i-th} = \Gamma_A (1 - (m-i)\Upsilon_A)$. The average OSN efficiency is $\eta_{OSN} = \frac{1}{m} \sum_{i=1}^m \eta_{OSN}^{i-th} = \Gamma_A (1 - \frac{1}{2}(m-1)\Upsilon_A)$, showing a linear decrease with m .

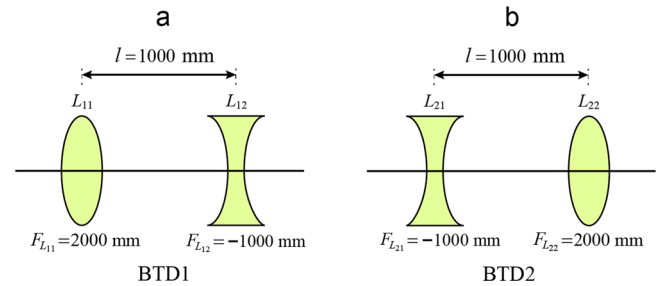


Fig. 6 Beam transformation devices (BTD). a Configurations of BTD1. **b** Configurations of BTD2.

Configuration of the PI (polarization interferometer) (see Fig. 5a) and cross sections of the array at different sites (see Fig. 5b). Beam transformation devices (BTDs). In the experiment, we used two BTDs (BTD1 and BTD2) to transform the beam array. The BTD1 (BTD2) is formed by a convex and a concave lens, denoted by L_{11} (L_{22}) and L_{12} (L_{21}), respectively, with L_{11} (L_{21}) placed on the left-hand side of L_{12} (L_{22}) (see Fig. 6). The focal lengths of the lenses L_{11} (L_{22}) and L_{12} (L_{21}) were chosen so that $F_{L11} = f_L(F_{L22} = f_L)$ and $F_{L12} = -f_L/F_{BTD}$ ($F_{L21} = -f_L/F_{BTD}$), with $f_L > 0$. The separation between L_{11} (L_{22}) and L_{12} (L_{21}) is $(1 - \frac{1}{F_{BTD}})f_L$. The ABCD matrix for BTD1 and BTD2 were calculated from

$$\begin{pmatrix} 1 & 0 \\ F_{BTD}/f_L & 1 \end{pmatrix} \begin{pmatrix} 1 & (1 - 1/F_{BTD})f_L \\ 0 & 1 \end{pmatrix} \begin{pmatrix} 1 & 0 \\ -1/f_L & 1 \end{pmatrix} = \begin{pmatrix} 1/F_{BTD} & (1 - 1/F_{BTD})f_L \\ 0 & F_{BTD} \end{pmatrix} \text{ and } \begin{pmatrix} 1 & 0 \\ -1/f_L & 1 \end{pmatrix} \begin{pmatrix} 1 & (1 - 1/F_{BTD})f_L \\ 0 & 1 \end{pmatrix} \begin{pmatrix} 1 & 0 \\ F_{BTD}/f_L & 1 \end{pmatrix} = \begin{pmatrix} F_{BTD} & (1 - 1/F_{BTD})f_L \\ 0 & 1/F_{BTD} \end{pmatrix}.$$

Therefore, when a beam array goes through the BTD1 (BTD2) from left- to right-hand side, it is shrunk (expanded) by factor F_{BTD} . In our current experiment, we used the lenses in hand, for which the focal lengths are $F_{L11} = 2000$ mm $F_{L22} = 2000$ mm, $F_{L12} = -1000$ mm, and $F_{L21} = -1000$ mm, which correspond to factor $F_{BTD} = 2$. In future work, one may increase (decrease) the factor F_{BTD} ($1/F_{BTD}$) by increasing (decreasing) the lens ratio $|F_{L11}/F_{L12}|$ ($|F_{L22}/F_{L21}|$).

Data availability

All data from this work are available through the corresponding author upon request.

Received: 23 January 2021; Accepted: 5 July 2021;

Published online: 22 July 2021

References

- Briegel, H. J., Dür, W., Cirac, J. I. & Zoller, P. Quantum repeaters: the role of imperfect local operations in quantum communication. *Phys. Rev. Lett.* **81**, 5932–5935 (1998).
- Sangouard, N., Simon, C., de Riedmatten, H. & Gisin, N. Quantum repeaters based on atomic ensembles and linear optics. *Rev. Mod. Phys.* **83**, 33–80 (2011).
- Simon, C. Towards a global quantum network. *Nat. Photon.* **11**, 678–680 (2017).
- Duan, L. M., Lukin, M. D., Cirac, J. I. & Zoller, P. Long-distance quantum communication with atomic ensembles and linear optics. *Nature* **414**, 413–418 (2001).
- Kimble, H. J. The quantum internet. *Nature* **453**, 1023–1030 (2008).
- Wehner, S., Elkouss, D. & Hanson, R. Quantum internet: a vision for the road ahead. *Science* **362**, eaam9288 (2018).
- Bussi eres, F. et al. Prospective applications of optical quantum memories. *J. Mod. Opt.* **60**, 1519–1537 (2013).
- Northup, T. E. & Blatt, R. Quantum information transfer using photons. *Nat. Photon.* **8**, 356–363 (2014).
- Lvovsky, A. I., Sanders, B. C. & Tittel, W. Optical quantum memory. *Nat. Photon.* **3**, 706–714 (2009).
- Volz, J. et al. Observation of entanglement of a single photon with a trapped atom. *Phys. Rev. Lett.* **96**, 030404 (2006).
- Reiserer, A. & Rempe, G. Cavity-based quantum networks with single atoms and optical photons. *Rev. Mod. Phys.* **87**, 1379–1418 (2015).
- Stanley, S. & Bloxham, J. Convective-region geometry as the cause of Uranus' and Neptune's unusual magnetic fields. *Nature* **428**, 151–153 (2004).
- Duan, L. M. & Monroe, C. Colloquium: quantum networks with trapped ions. *Rev. Mod. Phys.* **82**, 1209–1224 (2010).
- Hensen, B. et al. Loophole-free Bell inequality violation using electron spins separated by 1.3 kilometres. *Nature* **526**, 682–686 (2015).
- Delteil, A. et al. Generation of heralded entanglement between distant hole spins. *Nat. Phys.* **12**, 218–223 (2015).
- Kuzmich, A. et al. Generation of nonclassical photon pairs for scalable quantum communication with atomic ensembles. *Nature* **423**, 731–734 (2003).
- Chou, C. W. et al. Measurement-induced entanglement for excitation stored in remote atomic ensembles. *Nature* **438**, 828–832 (2005).
- Eisaman, M. D. et al. Electromagnetically induced transparency with tunable single-photon pulses. *Nature* **438**, 837–841 (2005).
- Laurat, J. et al. Efficient retrieval of a single excitation stored in an atomic ensemble. *Opt. Express* **14**, 6912–6918 (2006).
- Simon, J., Tanji, H., Thompson, J. K. & Vuletic, V. Interfacing collective atomic excitations and single photons. *Phys. Rev. Lett.* **98**, 183601 (2007).
- Felinto, D., Chou, C. W., de Riedmatten, H., Polyakov, S. V. & Kimble, H. J. Control of decoherence in the generation of photon pairs from atomic ensembles. *Phys. Rev. A* **72**, 053809 (2005).
- Laurat, J., Choi, K. S., Deng, H., Chou, C. W. & Kimble, H. J. Heralded entanglement between atomic ensembles: preparation, decoherence, and scaling. *Phys. Rev. Lett.* **99**, 180504 (2007).
- Zhao, B. et al. A millisecond quantum memory for scalable quantum networks. *Nat. Phys.* **5**, 95–99 (2008).
- Bao, X.-H. et al. Efficient and long-lived quantum memory with cold atoms inside a ring cavity. *Nat. Phys.* **8**, 517–521 (2012).
- Zhao, R. et al. Long-lived quantum memory. *Nat. Phys.* **5**, 100–104 (2008).
- Radnaev, A. G. et al. A quantum memory with telecom-wavelength conversion. *Nat. Phys.* **6**, 894–899 (2010).
- Yang, S.-J., Wang, X.-J., Bao, X.-H. & Pan, J.-W. An efficient quantum light-matter interface with sub-second lifetime. *Nat. Photon.* **10**, 381–384 (2016).
- Pang, X.-L. et al. A hybrid quantum memory-enabled network at room temperature. *Sci. Adv.* **6**, eaax1425 (2020).
- Zugenmaier, M., Dideriksen, K. B., Sørensen, A. S., Albrecht, B. & Polzik, E. S. Long-lived non-classical correlations towards quantum communication at room temperature. *Commun. Phys.* **1**, 1–7 (2018).
- Matsukevich, D. N. & Kuzmich, A. Quantum state transfer between matter and light. *Science* **306**, 663–666 (2004).
- de Riedmatten, H. et al. Direct measurement of decoherence for entanglement between a photon and stored atomic excitation. *Phys. Rev. Lett.* **97**, 113603 (2006).
- Chen, S. et al. Demonstration of a stable atom-photon entanglement source for quantum repeaters. *Phys. Rev. Lett.* **99**, 180505 (2007).
- Kutluer, K. et al. Time entanglement between a photon and a spin wave in a multimode solid-state quantum memory. *Phys. Rev. Lett.* **123**, 030501 (2019).
- Zhao, B., Chen, Z. B., Chen, Y. A., Schmiedmayer, J. & Pan, J. W. Robust creation of entanglement between remote memory qubits. *Phys. Rev. Lett.* **98**, 240502 (2007).
- Chen, Z. B., Zhao, B., Chen, Y. A., Schmiedmayer, J. & Pan, J. W. Fault-tolerant quantum repeater with atomic ensembles and linear optics. *Phys. Rev. A* **76**, 022329 (2007).
- Yuan, Z. S. et al. Experimental demonstration of a BDCZ quantum repeater node. *Nature* **454**, 1098–1101 (2008).
- Matsukevich, D. N. et al. Entanglement of a photon and a collective atomic excitation. *Phys. Rev. Lett.* **95**, 040405 (2005).
- Dudin, Y. O. et al. Entanglement of light-shift compensated atomic spin waves with telecom light. *Phys. Rev. Lett.* **105**, 260502 (2010).
- Yang, S. J. et al. Highly retrievable spin-wave-photon entanglement source. *Phys. Rev. Lett.* **114**, 210501 (2015).
- Ding, D.-S. et al. Raman quantum memory of photonic polarized entanglement. *Nat. Photon.* **9**, 332–338 (2015).
- Wu, Y. L. et al. Simultaneous generation of two spin-wave-photon entangled states in an atomic ensemble. *Phys. Rev. A* **93**, 052327 (2016).
- Farrera, P., Heinze, G. & de Riedmatten, H. Entanglement between a photonic time-bin qubit and a collective atomic spin excitation. *Phys. Rev. Lett.* **120**, 100501 (2018).
- Saglamyurek, E. et al. Broadband waveguide quantum memory for entangled photons. *Nature* **469**, 512–515 (2011).
- Clausen, C. et al. Quantum storage of photonic entanglement in a crystal. *Nature* **469**, 508–511 (2011).
- Saglamyurek, E. et al. Quantum storage of entangled telecom-wavelength photons in an erbium-doped optical fibre. *Nat. Photon.* **9**, 83–87 (2015).
- Chen, Y.-A. et al. Memory-built-in quantum teleportation with photonic and atomic qubits. *Nat. Phys.* **4**, 103–107 (2008).
- Bussi eres, F. et al. Quantum teleportation from a telecom-wavelength photon to a solid-state quantum memory. *Nat. Photon.* **8**, 775–778 (2014).
- Bao, X. H. et al. Quantum teleportation between remote atomic-ensemble quantum memories. *Proc. Natl Acad. Sci. USA* **109**, 20347–20351 (2012).
- Yu, Y. et al. Entanglement of two quantum memories via fibres over dozens of kilometres. *Nature* **578**, 240–245 (2020).
- Razavi, M., Piani, M. & Lutkenhaus, N. Quantum repeaters with imperfect memories: cost and scalability. *Phys. Rev. A* **80**, 032301 (2009).
- Liu, X., Zhou, Z. Q., Hua, Y. L., Li, C. F. & Guo, G. C. Semihierarchical quantum repeaters based on moderate lifetime quantum memories. *Phys. Rev. A* **95**, 012319 (2017).
- Jiang, L., Taylor, J. M. & Lukin, M. D. Fast and robust approach to long-distance quantum communication with atomic ensembles. *Phys. Rev. A* **76**, 012301 (2007).
- Sangouard, N. et al. Robust and efficient quantum repeaters with atomic ensembles and linear optics. *Phys. Rev. A* **77**, 062301 (2008).
- Simon, C. et al. Quantum repeaters with photon pair sources and multimode memories. *Phys. Rev. Lett.* **98**, 190503 (2007).
- Collins, O. A., Jenkins, S. D., Kuzmich, A. & Kennedy, T. A. Multiplexed memory-insensitive quantum repeaters. *Phys. Rev. Lett.* **98**, 060502 (2007).
- Simon, C., de Riedmatten, H. & Afzelius, M. Temporally multiplexed quantum repeaters with atomic gases. *Phys. Rev. A* **82**, 010304 (2010).
- Sinclair, N. et al. Spectral multiplexing for scalable quantum photonics using an atomic frequency comb quantum memory and feed-forward control. *Phys. Rev. Lett.* **113**, 053603 (2014).
- Tian, L. et al. Spatial multiplexing of atom-photon entanglement sources using feedforward control and switching networks. *Phys. Rev. Lett.* **119**, 130505 (2017).
- Laplane, C., Jobez, P., Etesse, J., Gisin, N., & Afzelius, M. Multimode and long-lived quantum correlations between photons and spins in a crystal. *Phys. Rev. Lett.* **118**, 210501 (2017).
- Kutluer, K., Mazzer, M. & de Riedmatten, H. Solid-State source of nonclassical photon pairs with embedded multimode quantum memory. *Phys. Rev. Lett.* **118**, 210502 (2017).
- Seri, A. et al. Quantum correlations between single telecom photons and a multimode on-demand solid-state quantum memory. *Phys. Rev. X* **7**, 021028 (2017).
- Seri, A. et al. Quantum storage of frequency-multiplexed heralded single photons. *Phys. Rev. Lett.* **123**, 080502 (2019).
- Heller, L., Farrera, P., Heinze, G. & de Riedmatten, H. Cold-atom temporally multiplexed quantum memory with cavity-enhanced noise suppression. *Phys. Rev. Lett.* **124**, 210504 (2020).

64. Parniak, M. et al. Wavevector multiplexed atomic quantum memory via spatially-resolved single-photon detection. *Nat. Commun.* **8**, 2140 (2017).
65. Lan, S. Y. et al. A multiplexed quantum memory. *Opt. Express* **17**, 13639–13645 (2009).
66. Pu, Y. F. et al. Experimental realization of a multiplexed quantum memory with 225 individually accessible memory cells. *Nat. Commun.* **8**, 15359 (2017).
67. Chang, W. et al. Long-distance entanglement between a multiplexed quantum memory and a telecom photon. *Phys. Rev. X* **9**, 041033 (2019).
68. Wen, Y. et al. Multiplexed spin-wave-photon entanglement source using temporal multimode memories and feedforward-controlled readout. *Phys. Rev. A* **100**, 012342 (2019).
69. Li, C. et al. Quantum communication between multiplexed atomic quantum memories. *Phys. Rev. Lett.* **124**, 240504 (2020).
70. Jiang, N. et al. Experimental realization of 105-qubit random access quantum memory. *NPJ Quantum Inf.* **5**, 28 (2019).
71. Dai, H. N. et al. Holographic storage of biphoton entanglement. *Phys. Rev. Lett.* **108**, 210501 (2012).
72. Heinze, G., Hubrich, C. & Halfmann, T. Stopped light and image storage by electromagnetically induced transparency up to the regime of one minute. *Phys. Rev. Lett.* **111**, 033601 (2013).
73. Ferguson, K. R., Beavan, S. E., Longdell, J. J. & Sellars, M. J. Generation of light with multimode time-delayed entanglement using storage in a solid-state spin-wave quantum memory. *Phys. Rev. Lett.* **117**, 020501 (2016).
74. Lipka, M., Mazelanik, M., Leszczyński, A., Wasilewski, W. & Parniak, M. Massively-multiplexed generation of Bell-type entanglement using a quantum memory. *Commun. Phys.* **4**, 46 (2021).
75. Vernaz-Gris, P., Huang, K., Cao, M., Sheremet, A. S. & Laurat, J. Highly-efficient quantum memory for polarization qubits in a spatially-multiplexed cold atomic ensemble. *Nat. Commun.* **9**, 363 (2018).
76. Wang, Y. et al. Efficient quantum memory for single-photon polarization qubits. *Nat. Photon.* **13**, 346–351 (2019).
77. England, D. G. et al. High-fidelity polarization storage in a gigahertz bandwidth quantum memory. *J. Phys. B- Mol. Opt.* **45**, 124008 (2012).
78. Cho, Y.-W. & Kim, Y.-H. Atomic vapor quantum memory for a photonic polarization qubit. *Opt. Express* **18**, 25786–25793 (2010).
79. Cho, Y. W. et al. Highly efficient optical quantum memory with long coherence time in cold atoms. *Optica* **3**, 100–107 (2016).
80. Wang, S. et al. Deterministic generation and partial retrieval of a spin-wave excitation in an atomic ensemble. *Opt. Express* **27**, 27409–27419 (2019).
81. Xu, Z. et al. Long lifetime and high-fidelity quantum memory of photonic polarization qubit by lifting zeeman degeneracy. *Phys. Rev. Lett.* **111**, 240503 (2013).
82. Surmacz, K. et al. Efficient spatially resolved multimode quantum memory. *Phys. Rev. A* **78**, 033806 (2008).
83. Matsukevich, D. N. et al. Deterministic single photons via conditional quantum evolution. *Phys. Rev. Lett.* **97**, 013601 (2006).
84. Chen, S. et al. Deterministic and storable single-photon source based on a quantum memory. *Phys. Rev. Lett.* **97**, 173004 (2006).
85. Albrecht, B., Farrera, P., Fernandez-Gonzalvo, X., Cristiani, M. & de Riedmatten, H. A waveguide frequency converter connecting rubidium-based quantum memories to the telecom C-band. *Nat. Commun.* **5**, 3376 (2014).
86. Ikuta, R. et al. Polarization insensitive frequency conversion for an atom-photon entanglement distribution via a telecom network. *Nat. Commun.* **9**, 1997 (2018).
87. van Leent, T. et al. Long-distance distribution of atom-photon entanglement at telecom wavelength. *Phys. Rev. Lett.* **124**, 010510 (2020).
88. Zhang, S. et al. A dark-line two-dimensional magneto-optical trap of 85Rb atoms with high optical depth. *Rev. Sci. Instrum.* **83**, 073102 (2012).
89. Hsiao, Y. F. et al. Highly efficient coherent optical memory based on electromagnetically induced transparency. *Phys. Rev. Lett.* **120**, 183602 (2018).

Acknowledgements

We acknowledge funding support from Key Project of the Ministry of Science and Technology of China (Grant No. 2016YFA0301402); The National Natural Science Foundation of China (Grants: No. 11475109, No. 11974228), Program for Shanxi Province; Fund for Shanxi “1331 Project” Key Subjects Construction.

Author contributions

H.W. conceived the research. H.W., Z.-X.X., S.-J.L., and S.-Z.W. designed the experiment. S.-Z.W., M.-J. W., Y.-F.W., T.-F.M. setup the experiment with assistances from all other authors. S.-Z.W., M.-J.W. took the data. S.-Z.W. analyzed the data. H.W. wrote the paper.

Competing interests

The authors declare no competing interests.

Additional information

Supplementary information The online version contains supplementary material available at <https://doi.org/10.1038/s42005-021-00670-9>.

Correspondence and requests for materials should be addressed to H.W.

Peer review information *Communications Physics* thanks the anonymous reviewers for their contribution to the peer review of this work. Peer reviewer reports are available.

Reprints and permission information is available at <http://www.nature.com/reprints>

Publisher's note Springer Nature remains neutral with regard to jurisdictional claims in published maps and institutional affiliations.



Open Access This article is licensed under a Creative Commons Attribution 4.0 International License, which permits use, sharing, adaptation, distribution and reproduction in any medium or format, as long as you give appropriate credit to the original author(s) and the source, provide a link to the Creative Commons license, and indicate if changes were made. The images or other third party material in this article are included in the article's Creative Commons license, unless indicated otherwise in a credit line to the material. If material is not included in the article's Creative Commons license and your intended use is not permitted by statutory regulation or exceeds the permitted use, you will need to obtain permission directly from the copyright holder. To view a copy of this license, visit <http://creativecommons.org/licenses/by/4.0/>.

© The Author(s) 2021